

A Three-Dimensional Multiphysics Coupled Model of Melting and Rotation of the Electrode During Electroslag Remelting Process



XUECHI HUANG, ZHONGQIU LIU, BAOKUAN LI, FANG WANG,
and CHENGJUN LIU

A transient three-dimensional (3D) coupled model is developed to investigate the melting and rotation of the solid electrode during the electroslag remelting (ESR) process. The large eddy simulation (LES) method is utilized to model the multiphase flow. The slag/metal interface is precisely tracked utilizing the volume of fluid (VOF) approach with an adaptive mesh refinement strategy. The model pays specific attention to the shape evolution of the electrode tip, as well as the formation and motion of droplet under different electrode rotating speeds. The accuracy of the model is validated by an additional transparent experiment. As the electrode rotates, the centrifugal force pushes the randomly dispersed faucets underneath the electrode outwards until reaching the periphery. The electrode rotation flattens the electrode tip, reducing the horizontal deviation of its profile by up to 69.9 pct compared to a static electrode. As the electrode rotating speed increases from 0 to 60 rpm, the thickness of liquid metal film decreases from 0.91 to 0.63 mm, while the equivalent diameter of droplets decreases from 12.90 to 11.77 mm. The electrode rotation increases the specific surface area, dramatically improving the removal efficiency of inclusions and harmful elements. Moreover, productivity reached a maximum of 21.56 pct at a rotating speed of 60 rpm without increasing power input.

<https://doi.org/10.1007/s11663-024-03013-5>

© The Minerals, Metals & Materials Society and ASM International 2024

I. INTRODUCTION

ELECTROSLAG remelting (ESR) is a vital secondary refining process widely used in the production of high-performance steels and alloys required for hot-end components of aircraft engines,^[1] nuclear power main pipelines,^[2,3] and turbine rotors,^[4] among others. As illustrated in Figure 1, the ESR system typically includes an AC power source, short circuit, consumable electrode, slag, ingot, and water-cooled mold. When the power supply circuit is activated, the current flows through the high-resistance slag, generating a large amount of Joule heat. This keeps the slag in an overheated molten state, enabling the heating and subsequent melting of the consumable electrode. The molten electrode metal aggregates and forms one or more liquid metal faucets. The gravity and Lorentz force

split the faucets into droplets, which fall through the slag pool and subsequently solidify upward inside the mold. A servo motor, operating throughout the remelting process, dynamically adjusts the vertical motility of the electrode to accommodate variations in the depth of the slag pool. This ensures maintaining a constant immersion depth for the electrode in the slag pool.

The purification process of ESR occurs at the slag–metal interface,^[5] including the removal of inclusions,^[6] desulfurization,^[7,8] deoxidation,^[9,10] among other. During the formation of liquid metal films and subsequent collection into metal droplets at the electrode tip, a significant quantity of inclusions is efficiently removed, accounting for approximately 2/3 of the overall removal.^[11,12] In contrast, the stage where the droplets pass through the slag pool and subsequently collect into the liquid metal pool plays a less role. The primary factor is that the contact area between the slag and the metal at the electrode tip is much larger than at other positions, leading to more inclusions being adsorbed by the slag. Therefore, a comprehensive understanding of the melting of the electrode metal and droplet evolution behavior is crucial for enhancing the purification efficiency of the ESR process.

XUECHI HUANG and CHENGJUN LIU are with the Key Laboratory for Ecological Metallurgy of Multimetallic Ores, Northeastern University, Shenyang 110819, P.R. China and also with the School of Metallurgy, Northeastern University, Shenyang 110819, P.R. China. Contact e-mail: huangxuechi@smm.neu.edu.cn ZHONGQIU LIU, BAOKUAN LI, and FANG WANG are with the School of Metallurgy, Northeastern University. Contact e-mail: liuzq@smm.neu.edu.cn

Manuscript submitted July 31, 2023; accepted January 8, 2024.

Article published online February 28, 2024.

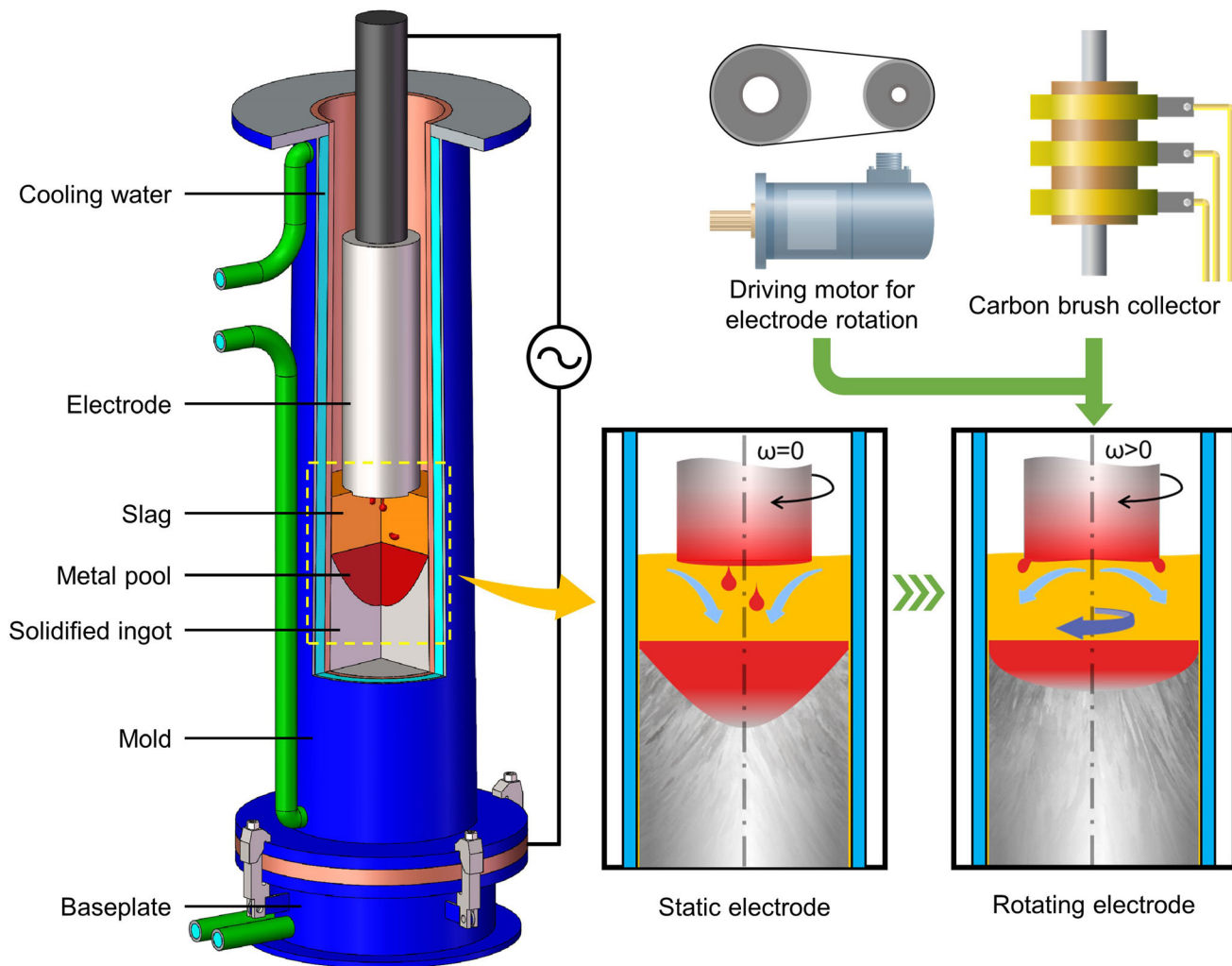


Fig. 1—Schematic of the ESR process with a rotating electrode.

The innovative rotating electrode method in the ESR process has been proposed in Reference 13. As illustrate in Figure 1, the electrode descends in the axial direction while rotating along the axis at a fixed angular speed. The centrifugal force causes the molten metal to move outwards, counter to the electromagnetic force induced by AC. This results in the formation of liquid metal faucets at the periphery of the electrode, from which smaller droplets are released. Chumanov *et al.*^[14] concluded that the utilization of rotating electrodes increases the melting rate (by more than 25 pct in some cases) without increasing the power input. There exists an optimal rotating speed for the electrode that maximizes productivity within the given process parameters. Concurrently, an increase in rotating speed leads to a decrease in the thickness of the liquid metal film. Consequently, nonmetallic inclusions are more likely to be located at the phase boundary and subsequently assimilated by the slag. Demirci *et al.*^[15] experimentally

confirmed that the number of visible faucets at the electrode tip increases with the rotating speed, specifically 7 at 20 rpm and 11 at 50 rpm.

Experimental observations and measurements of the melting electrode and droplets are challenging due to the opaque reactors and the elevated temperatures involved. However, numerical studies utilizing computational power and mathematical models have provided valuable insights into these processes.^[16–18] Kharicha *et al.*^[19] employed a multiphase-magnetohydrodynamic (MHD) approach to simulate droplet formation during electrode melting, revealing the non-axisymmetric flow pattern induced by the movement of droplets in the slag pool. Karimi-Sibaki *et al.*^[20] observed that the high-temperature slag first melts the periphery of the electrode, resulting in a parabolic-like shape at the electrode tip under the action of the slag flow. Wang *et al.*^[21,22] found that an external transverse static magnetic field can break the droplet neck into multiple smaller droplets

through strong periodic inverse Lorentz forces. This increases the slag–metal interface area and reduces the migrating distance of inclusions, thus improving purifying efficiency. Wang *et al.*^[23] compared the vibrating and traditional electrodes in the ESR furnace and concluded that horizontal vibration in the electrode reduces the droplet diameter. However, the effect of electrode rotation on the shape of the electrode tip and the droplet formation during the melting of consumable electrodes has been rarely reported, limiting the practical application of rotating electrode technology.

In the current study, a three-dimensional (3D) multiphysics coupled mathematical model is constructed, with a specific focus on the melting and rotation of the solid electrode. The slag/metal interface is precisely tracked utilizing the volume of fluid (VOF) approach in conjunction with an adaptive mesh refinement strategy. The electromagnetic field, multiphase flow, and heat transfer are simultaneously resolved. The study explores the shape evolution of the electrode tip and the formation and subsequent movement of droplets under four distinct electrode rotating speeds.

II. MODEL DESCRIPTION

The electromagnetic field, fluid flow, and heat transfer are simulated using the commercial CFD software ANSYS Fluent with a finite volume method (FVM). The 3D calculation domain encompasses the solid electrode, molten slag layer, and liquid metal pool. Given their efficiency and accuracy of the calculations, this study focuses on the melting of electrodes and droplet formation, disregarding the solidification of the ingot. The molten slag and liquid metal are assumed to be incompressible Newtonian fluids. Moreover, the ESR process is assumed to be in a quasi-steady state with an unchanged power supply regime.

A. Governing Equations

1. Electromagnetic field

The AC-induced electromagnetic field is solved by the A – ϕ formulation, which is derived from Maxwell's equations.^[24] This formulation exhibits exceptional sturdiness in situations involving a moving interface where the electric conductivity breaks. The effects of the current displacement and the magnetic convection are negligible.^[25,26] The current density distribution is determined by the current continuity equation and Ohm's law:

$$\nabla \cdot \vec{J} = 0, \quad [1]$$

$$\vec{J} = -\sigma \frac{\partial \vec{A}}{\partial t} - \sigma \nabla \phi, \quad [2]$$

where \vec{J} is the current density. σ is the electrical conductivity. \vec{A} is the magnetic vector potential. ϕ is the electric scalar potential.

The induced magnetic field is calculated by the A equation and the constitutive relation:

$$\nabla \times \vec{H} = \vec{J}, \quad [3]$$

$$\vec{B} = \mu_0 \vec{H} = \nabla \times \vec{A}, \quad [4]$$

where \vec{H} is the magnetic field intensity. \vec{B} is the magnetic flux density. μ_0 is the magnetic permeability.

Subsequently, the time-averaged Lorentz force \vec{F}_e and Joule heating Q_J can be deduced and interpolated as source terms for the momentum and energy conservation equations, respectively.

$$\vec{F}_e = \vec{J} \times \vec{B}, \quad [5]$$

$$Q_J = \frac{\vec{J} \cdot \vec{J}}{\sigma}. \quad [6]$$

2. Multiphase flow

The VOF approach is employed for explicit resolution of the redistribution of slag and metal phases.^[27] The slag/metal interface, where the volume fractions range from 0 to 1, is reconstructed at each iteration. The properties of the mixture phase can be computed by employing an ensemble averaging technique based on the local volume fractions. The surface tension is modeled by the continuum surface force (CSF) model.

$$\frac{\partial \alpha_m}{\partial t} + \nabla \cdot (\vec{v} \alpha_m) = 0, \quad [7]$$

$$\bar{\phi} = \phi_m \alpha_m + \phi_s (1 - \alpha_m), \quad [8]$$

where α_m denotes the volume fraction of the metal. ϕ is the property.

In this study, the large eddy simulation (LES) method is utilized to model the multiphase flow.^[19,28] In contrast to Reynolds average Navier–Stokes (RANS) models, the LES model offers enhanced flow detail representation while maintaining an acceptable computational cost. The continuity equation and govern the flow.

$$\frac{\partial \rho}{\partial t} + \nabla \cdot (\rho \vec{v}) = 0, \quad [9]$$

$$\begin{aligned} \frac{\partial(\rho \vec{v})}{\partial t} + \nabla \cdot (\rho \vec{v} \vec{v}) = & -\nabla p + \mu_{\text{eff}} \nabla^2 \vec{v} + \vec{F}_e + \vec{F}_b + \vec{F}_{\text{st}} \\ & + \vec{F}_{\text{damp}}, \end{aligned} \quad [10]$$

where μ_{eff} is the effective viscosity, as a sum of the molecular viscosity μ and turbulent viscosity μ_t . \vec{F}_b is the buoyancy force defined by the Boussinesq approximation.^[29] \vec{F}_{st} is the surface tension.^[30] \vec{F}_{damp} denotes the damping force in the mushy zone.^[12]

The subgrid-scale turbulent stress τ_{ij} is computed from:

$$\tau_{ij} = \frac{1}{3} \tau_{kk} \delta_{ij} - 2\mu_t \bar{S}_{ij}, \quad [11]$$

where τ_{kk} represents the isotropic part of the subgrid-scale stress. δ_{ij} is the Kronecker delta. \bar{S}_{ij} is the rate-of-strain tensor. The turbulent viscosity is modeled by the Smagorinsky–Lilly model:

$$\mu_t = \rho L_s^2 |\bar{S}|, \quad [12]$$

where $|\bar{S}|$ is the additional stress term, $|\bar{S}| = \sqrt{2\bar{S}_{ij}\bar{S}_{ij}}$.

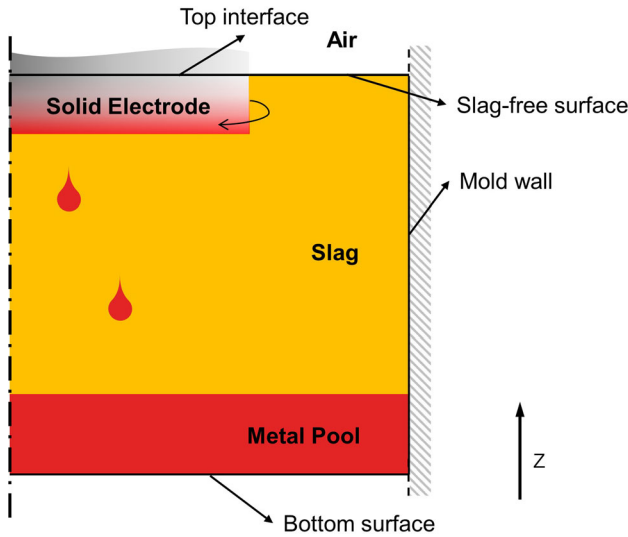


Fig. 2—Required boundaries in the present study.

L_S is the mixing length for subgrid scales:

$$L_S = \min(\kappa d, C_S V^{1/3}), \quad [13]$$

where κ is the von Kármán constant. d is the distance to the closest wall. C_S is the Smagorinsky constant. V is the volume of the computational cell.

3. Heat transfer

The temperature distribution is determined by solving an enthalpy (H) conservation equation^[31]:

$$\frac{\partial}{\partial t}(\rho H) + \nabla \cdot (\vec{v}\rho H) = \nabla \cdot (k_{eff}\nabla T) + Q_J, \quad [14]$$

where k_{eff} is the effective thermal conductivity including the turbulent effect, $k_{eff} = bc_p\mu_{eff}$. b is the inverse Prandtl number. c_p is the specific heat.

The melting of the electrode metal is solved implicitly using the enthalpy–porosity model. In this model, the liquid–solid mushy zone is considered as a porous region, where the porosity decreases from 0 to 1 as the metal melts.

$$H = \int_{T_{ref}}^T c_p dT + f_l L, \quad [15]$$

$$\begin{cases} f_l = 0, & \text{if } T \leq T_{solidus}, \\ f_l = \frac{T - T_{solidus}}{T_{liquidus} - T_{solidus}}, & \text{if } T_{solidus} < T < T_{liquidus}, \\ f_l = 1, & \text{if } T \geq T_{liquidus}, \end{cases} \quad [16]$$

where f_l is the liquid fraction. L is the latent heat of fusion. $T_{liquidus}$ and $T_{solidus}$ represent the liquidus temperature and solidus temperature, respectively.

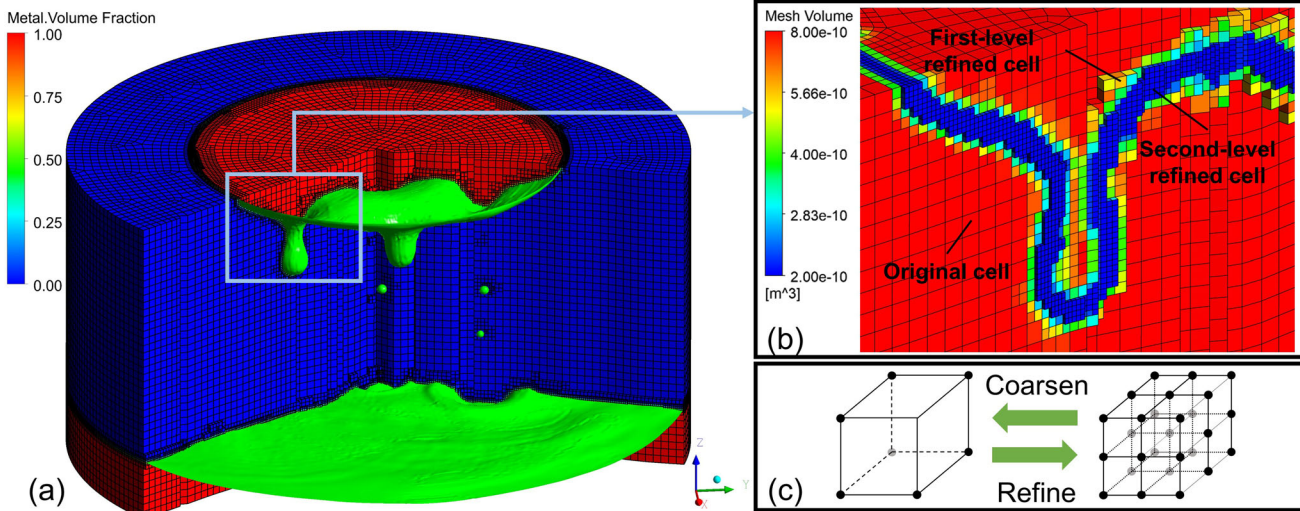


Fig. 3—Schematic of adaptive mesh refinement. (a) Mesh and the slag/metal interface, (b) refinement layers, and (c) refining and coarsening of hexahedron.

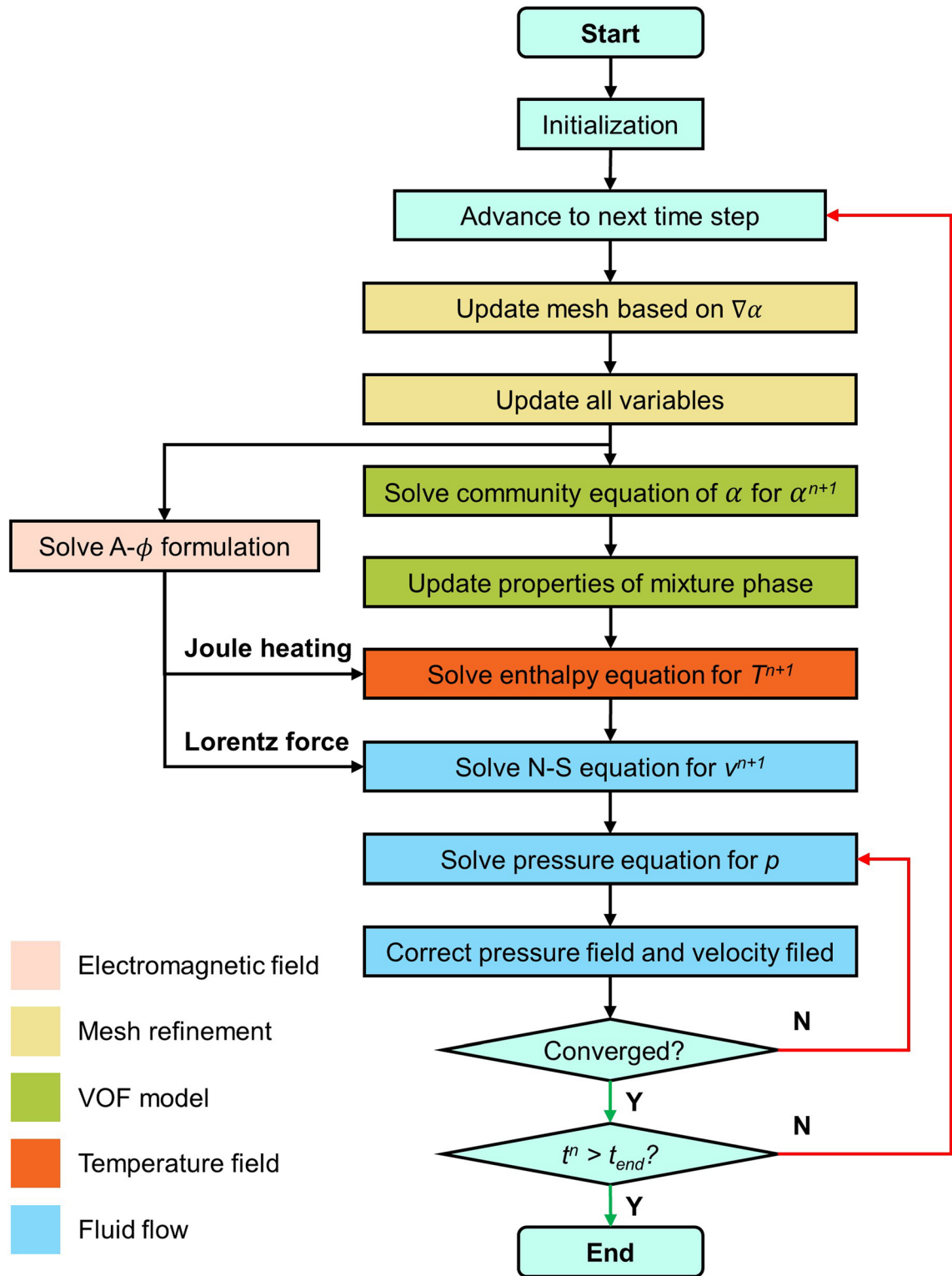


Fig. 4—Solution sequence for the coupled multi-physical fields.

B. Boundary Conditions

The computational boundaries are shown in Figure 2. The solid electrode is positioned on top of the slag layer at a fixed immersion depth. The alternative current flows between the electrode and the baseplate. It is assumed

that the solidified slag skin completely blocks the current from entering the mold, resulting in electrical insulation of the melt from the mold.^[27] Consequently, the potential gradient at the slag-free surface and the mold wall is set to zero. A zero potential is imposed at the

Table I. Material Properties and Process Parameters

Material Properties	H13 Die Steel	CaF ₂ -CaO-Al ₂ O ₃ Slag
Density (kg/m ³)	7500	2600
Viscosity (mPa·s)	6.6 (1730 K), 6.0 (1800 K), 5.2 (1900 K), 4.4 (2000 K)	55.1 (1600 K), 30.1 (1800 K), 17.5 (2000 K)
Specific Heat (J/kg·K)	830	1255
Thermal Conductivity (W/m·K)	30.5	~ 10.5
Electrical Conductivity [1/(Ω·m)]	7.0 × 10 ⁵	lnσ = 11.796 - 11,513/T
Liquidus/Solidus (K)	1730/1636	—
Latent Heat of Fusion (kJ/kg)	270	—
Thermal Expansion Coefficient (1/K)	2.0 × 10 ⁻⁴	1.0 × 10 ⁻⁴
Surface Tension Coefficient (N/m)	0.9	—
Process Parameters		
Electrode Diameter (mm)	120	—
Mold Diameter (mm)	200	—
Slag Height (mm)	80	—
Initial Immersion Depth of Solid Electrode (mm)	20	—
Current (kA)	3.2	—
Frequency (Hz)	50	—
Heat Transfer at Mold Wall (W/m ² ·K)	~ 400	—
Heat Transfer at Slag-Free Surface (W/m ² ·K)	~ 80	—
Emissivity of Slag at Slag-Free Surface	0.6	—

bottom surface, while a potential gradient is specified at the top interface of the electrode (Eq. [17]). Additionally, the influence of AC skin effect is taken into consideration.

$$\frac{\partial \phi}{\partial z} = \frac{I_{\text{rms}} \exp\left(\frac{r-r_{\text{max}}}{\delta}\right)}{\sigma \pi r_{\text{max}}^2}, \quad \delta = \sqrt{\frac{\rho_{\text{em}}}{\mu_{0\text{m}} \pi f_{\text{H}}}}, \quad [17]$$

where I_{rms} is the root mean square current. r_{max} is the electrode radius. δ is electromagnetic skin depth. ρ_{em} is the resistance of metal. $\mu_{0\text{m}}$ is the vacuum permittivity. f_{H} is the current frequency.

The magnetic flux density is continuous at the bottom surface and other horizontal boundaries (Eq. [18]), while it is set to zero at the mold wall (Eq. [19]).

$$A_x = A_y = \frac{\partial A_z}{\partial z} = 0, \quad [18]$$

$$A_x = A_y = A_z = 0. \quad [19]$$

Initially, the solid electrode region is assigned manually. To enable the rotation of the solid electrode, an additional pulling angular velocity is imposed to this region. The pulling velocity remains effective until the electrode in this position is completely melted. Accordingly, a non-slip condition is enforced at the mold wall and the upper interface of the electrode. A zero-shear stress condition is imposed at the slag-free surface in contact with the surrounding atmosphere. The bottom surface is considered as the solidification front, where no reverse flow occurs.

Heat convection and radiation are considered at the slag-free surface. Heat transfer at the mold wall is a complex process involving contact resistance, heat conduction in the solidified slag skin, heat convection,

and radiation in the air gap resulting from ingot shrinkage. This heat transfer process is also influenced by its localization and progression, and there are currently insufficient parameters available to describe it comprehensively. Therefore, equivalent heat transfer coefficients are used to account for the complex heat transport.^[12,20]

C. Adaptive Mesh Refinement

The droplet diameter typically ranges from 10 to 15 mm, which can be influenced by various factors including surface tension.^[19] In the VOF approach, the slag/metal interface is solved by requiring at least one layer of the grid, where the phase fraction varies from 0 (slag phase) to 1 (metal phase). Adaptive mesh refinement is employed to dynamically refine the mesh around the interface, thereby accurately describing the droplet profiles.

During the adaption process, individual cells are first marked for refinement or coarsening based on the following gradient criteria: the mesh around the interface, where the absolute value of the volume fraction gradient exceeds a predetermined threshold, is marked for refinement. Otherwise, meshes are considered for coarsening. The current calculations set the threshold at 0.1. Cells marked for refinement are then divided, as shown in Figure 3, for example, a hexahedron is split into eight hexahedra. To maintain higher accuracy, neighboring cells are not allowed to differ by more than one level of refinement. This prevents excessive variations in cell volume (reducing truncation error) and ensures that the positions of the parent (original) and child (refined) cell centroids are similar (reducing errors in flux calculations).

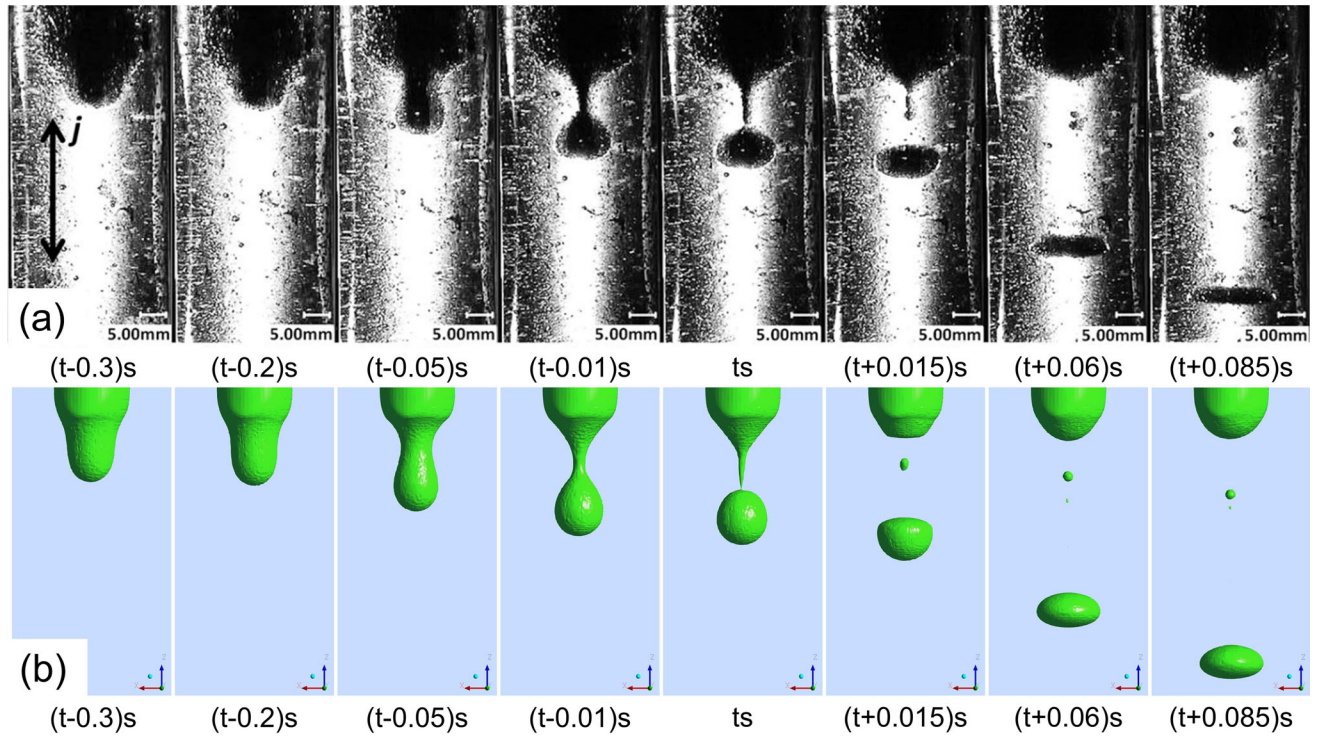


Fig. 5—Zinc droplet formation during ESR process (a) experimental results^[21] and (b) simulated results.

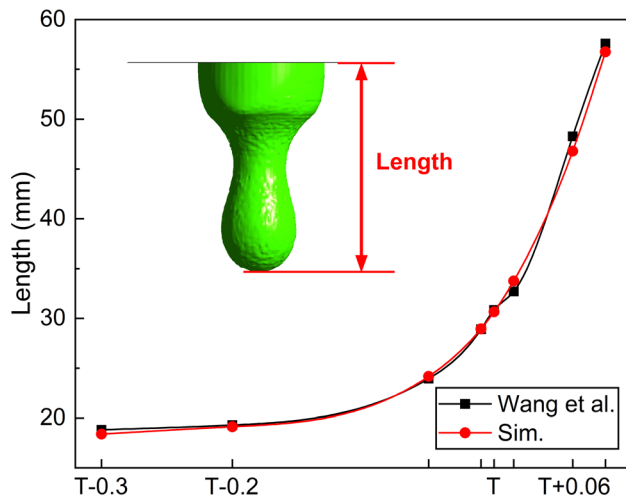


Fig. 6—Variation of the droplet length over time during the droplet formation process.

The mesh can be coarsened following refinement. An inactive parent cell is reintroduced and reactivated if all its child cells are marked for coarsening. This process allows for the restoration of the original mesh. It should be noted that further coarsening of the original mesh is not possible. The default maximum refinement level for splitting cells during adaptation is set to 2. Dynamic adaptation is executed before each iteration.

III. NUMERICAL DETAILS

Figure 4 illustrates the solution sequence for the coupled multi-physics fields. During each iteration, the adaptive mesh refinement is first executed, and all parameters of each cell are updated. Utilizing the temperature-dependent electrical conductivity and the phase fraction distribution, the electromagnetic field is solved by the user defined functions (UDFs). The calculated Lorentz force and Joule heating density are then incorporated into the momentum and energy conservation equations as source terms. In addition, physical properties such as conductivity and certain boundary conditions are achieved through UDFs. The Semi-Implicit Method for Pressure-Linked Equations (SIMPLE) algorithm is adopted to solve the N-S equations and pressure Poisson equation. The multi-phase-specific time stepping algorithm is used to calculate the transient flow. The global time step is adaptively changed based on the global Courant number, with a maximum value of 0.3 for accurate instantaneous-time solutions. After conducting a mesh independence test, the computational domain is divided into structural grids with a primary size of 2.5 mm. The transient calculation requires approximately 160 CPU hours per case through parallel computing on a 64-core 2.8 GHz cluster.

The ESR process of H13 die steel is simulated at four different electrode rotating speeds. The slag composition consists of 50 wt pct CaF_2 , 25 wt pct CaO , and 25 wt pct Al_2O_3 . Table I^[32–34] list the main physical properties and process parameters required for calculations.

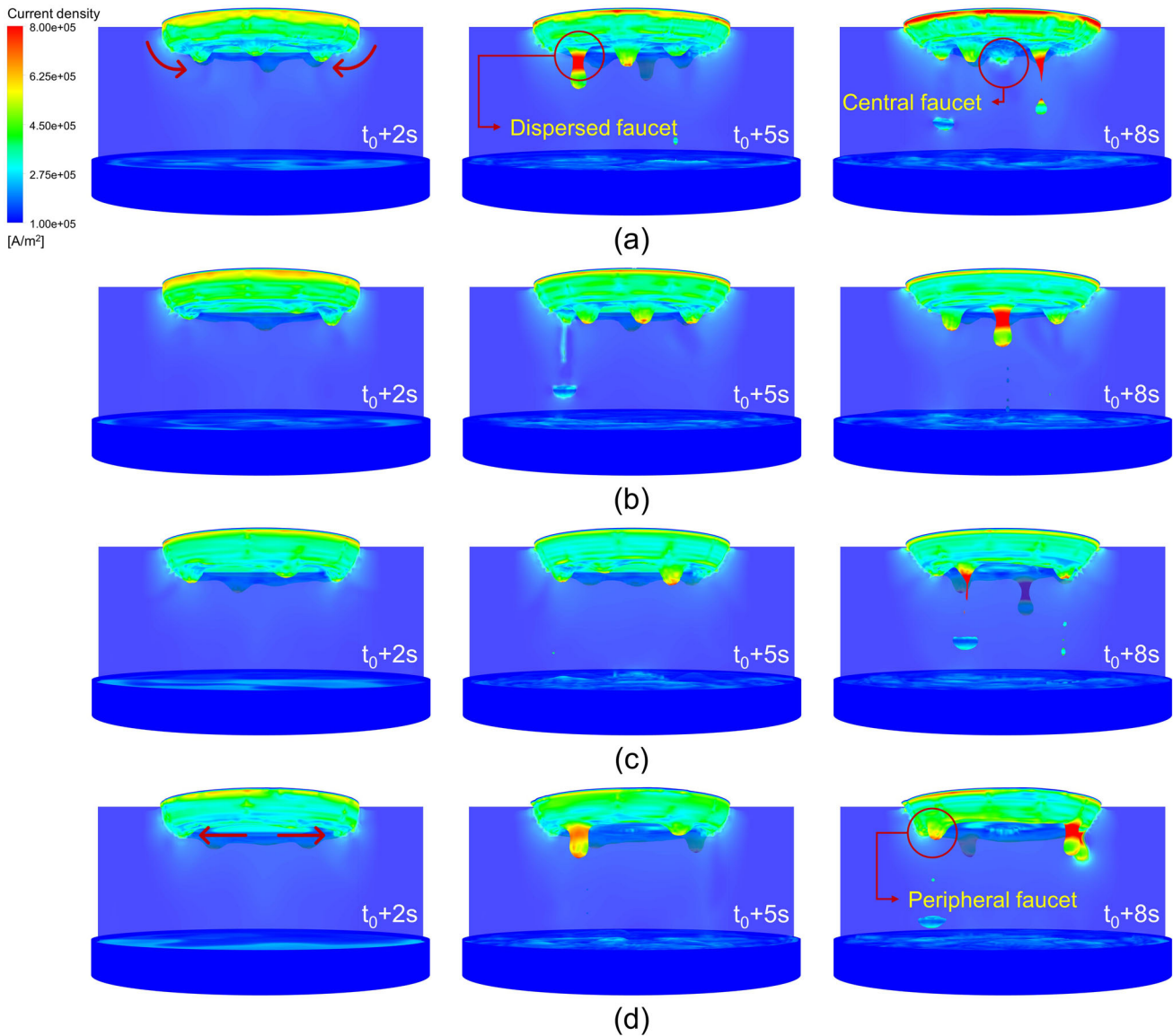


Fig. 7—Evolutions of formation and departure of droplets under the electrode rotating at (a) 0, (b) 20 rpm, (c) 40 rpm, and (d) 60 rpm.

IV. RESULTS AND DISCUSSION

A. Model Validation

To validate the model, a comparison is made between the simulated and experimental results. Wang *et al.*^[21] developed a transparent physical model to visualize the evolution of molten droplets at the electrode tip. They used a zinc bar as the consumable electrode, molten $ZnCl_2$ as the slag, and a quartz glass tube as the mold, enabling the entire process to be observed. In this paper, we independently simulate this process using the coupled model, as shown in Figure 5. The molten zinc film gradually aggregates to form a droplet, which detaches from the electrode at T s. The larger droplet (primary droplet) falls downwards while the neck breaks off into smaller droplets (satellite droplets). The simulated process closely resembles the experimental observations. However, the transparency of the glass tube may affect the observation due to the lensing effect. The molten

zinc in the quartz tube appears horizontally elongated in comparison to its true form. The simulated and experimental droplet lengths (the distance between the droplet bottom and the slag-free surface) were compared, as illustrated in Figure 6. The two are in good agreement, confirming the accuracy of the coupled model. The deviation attributes to uncertainties in the experimental observations and the uncertainty of the material properties and boundary conditions.

B. Electrical Heating and Electrode Melting

Figure 7 shows the formation and departure of droplets under different electrode rotating speeds. The slag-metal interface is colored by the current density magnitude. When the current circuit is activated, the current primarily flows through the metal phase with low resistivity. In the case with a static electrode is used (as shown in Figure 7(a)), the AC skin effect leads to

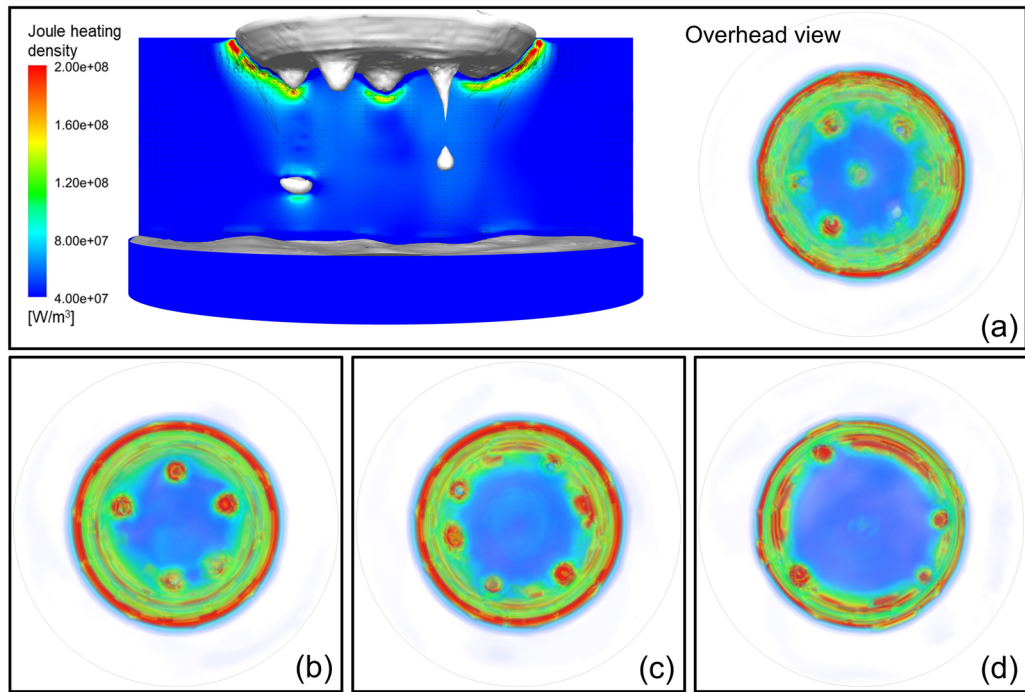


Fig. 8—Predicted distribution of time-averaged Joule heating density under different electrode rotating speeds at $t_0 + 8$ s: (a) 0, (b) 20 rpm, (c) 40 rpm, and (d) 60 rpm. Overhead views are shown in volume rendering.

higher current density at the periphery of the solid electrode. Due to the much greater skin depth in the slag, the distribution of current density is relatively uniform. As a result, the metal at the periphery of the electrode melts first. The molten metal then converges towards the center under the combined influence of gravity and Lorentz forces. As the liquid metal film thickens, several randomly dispersed faucets and a central faucet form at the electrode tip. The faucets are elongated by the surface tension and gravity. During the elongation, the current density sharply increases to minimize resistance. This induces powerful electromagnetic pinch forces, which break the elongated faucet into a primary droplet and subsequently satellite droplets. Once the droplet detaches, the current density within it abruptly decreases.

As the electrode rotates, the molten metal is subjected to the centrifugal force in the opposite direction to the Lorentz force. This centrifugal effect hinders the inward convergence of the molten metal, causing the dispersed faucets to move slightly outward with the electrode rotating at 20 rpm (Figure 7(b) illustrates this). It is noticeable that there is no central faucet formed, as distinct from the case with a static electrode. The locations of faucets depend on the competition between the Lorentz force and the centrifugal force. When the rotating speed increases to 40 and 60 rpm, the centrifugal force becomes the dominant driving force for the motion of liquid metal at the electrode tip. All the faucets form at the periphery of the electrode tip. Consequently, the droplets are randomly thrown out at the periphery, as shown in Figures 7(c) and (d).

The Joule heating required to melt the solid electrode is calculated using Eq. [6]. A large amount of Joule heating is generated in the slag, which has a resistivity three orders of magnitude higher than that of the metal, as displayed in Figure 8(a). When viewed from above, the Joule heating is concentrated in the slag directly beneath the electrode. The region with a high Joule heating density is located underneath the periphery of the electrode. Additionally, a substantial amount of Joule heating is generated around the faucets. Consequently, as the rotating speed increases from 0 to 60 rpm, the internal heat sources migrate from the interior towards the periphery (Figures 8(a) through (d) illustrates this migration).

C. Magnetohydrodynamic Flow and Heat Transfer

The N-S equations consider thermal buoyancy and Lorentz force as additional volumetric forces that drive local flows. Using the LES model, this study captures a highly detailed flow structure. As seen in Figure 9(a), when a static electrode is employed, the Lorentz force drives the slag near the electrode tip towards the faucets at a relatively slow velocity. The falling droplets drag downwards the slag in their vicinity, resulting in upward backflows beneath the electrode. Due to the dispersed manner of the falling droplets, the vortex below the electrode is constantly changing. Simultaneously, the thermal buoyancy dominates the descending flow near the mold. When the electrode rotates (as shown in Figure 9(b)), the liquid metal underneath the electrode tip moves accordingly. Specifically, the liquid metal

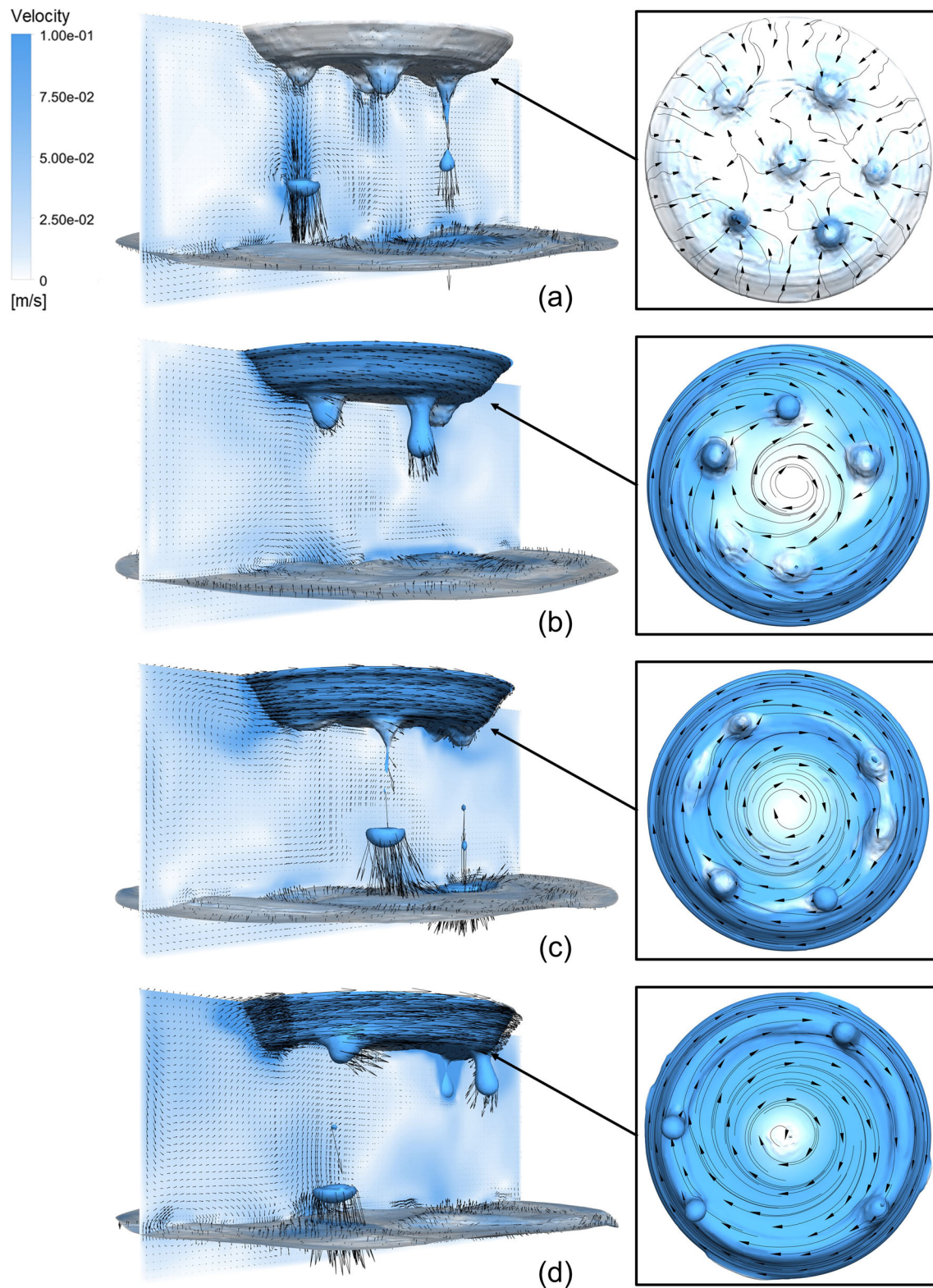


Fig. 9—Predicted fluid flow under different electrode rotating speeds at $t_0 + 8$ s: (a) 0, (b) 20 rpm, (c) 40 rpm, and (d) 60 rpm.

exhibits an inward spiral flow at the periphery of the electrode tip and an outward spiral flow at the center. With the increasing rotating speed, the outward spiral flow expands until the peripheral faucets are formed, as

shown in Figures 9(c) and (d). Horizontal tangential velocity is observed at the elongated faucets. However, the slag blocks the horizontal motion of the droplets. Prior to falling into the liquid metal pool, the horizontal

velocity of the droplet is relatively low. More importantly, the shear stress induced by the electrode rotation drives a strong swirling flow in the slag layer. The swirling flow gradually weakens with depth.

Figure 10 presents the effect of electrode rotation on key flow variables over a statistical period. As the electrode rotating speed varies from 0 to 60 rpm, the maximum velocity of the melt increases from 0.423 to 0.619 m/s, while the averaged vorticity of the slag layer increases from 3.04 to 6.51 s⁻¹. This indicates that electrode rotation dramatically intensifies the flow in the slag layer. However, its effect on the liquid metal pool is comparatively minimal. In comparison to the static case,

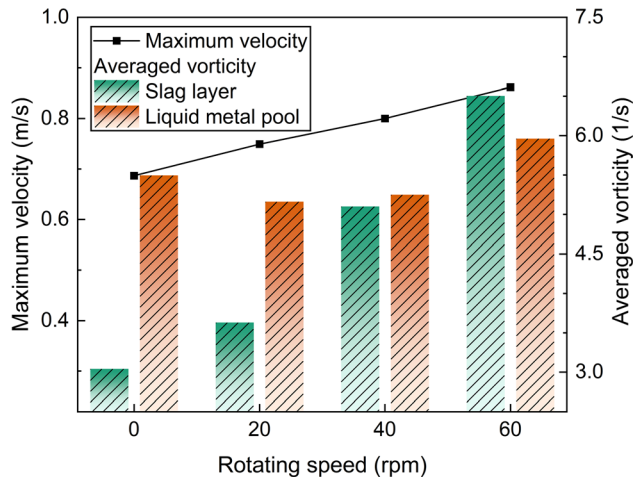


Fig. 10—Maximum velocity and averaged vorticity of the melt under different electrode rotating speeds.

the vorticity of the liquid metal pool weakens at lower rotating speeds (20 and 40 rpm) due to smaller droplets. The flow strengthens until the electrode rotates at a higher rotating speed (60 rpm).

The temperature distribution is influenced by fluid flow, Joule heating, and thermal conductivity, as depicted in Figure 11. In the case with a static electrode, the hottest region is observed in the upper slag layer due to dominant Joule heating. Some of the heat is used to heat and melt the solid electrode, causing a noticeable temperature gradient in the vicinity of the electrode. Additionally, heat is dissipated through cooling boundaries like the mold and atmosphere. The droplets drag the hotter slag downward, while the descending vortex near the mold expands the high-temperature region. As the electrode rotating speed increases, the hottest region gradually migrates outwards, transitioning from a convex shape to an arched shape. The averaged effective thermal conductivity rises from 16.29 to 17.11 W/m·K as the electrode rotating speed varies from 0 to 60 rpm. In other words, the electrode rotation enhances the global heat convection and diffusion in the melt. The maximum temperatures recorded are 2022 K, 2017 K, 1987 K, and 1953 K for electrode rotating speed of 0, 20, 40, and 60 rpm, respectively. This attributes to a stronger heat transfer between the electrode and the slag, as well as between the melt and the mold.

D. Electrode Tip Shape

As discussed above, the electromagnetic field, velocity field, temperature field, and electrode tip shape interact dynamically. The voltage drop and subsequently power consumption and heat generation depend on both the

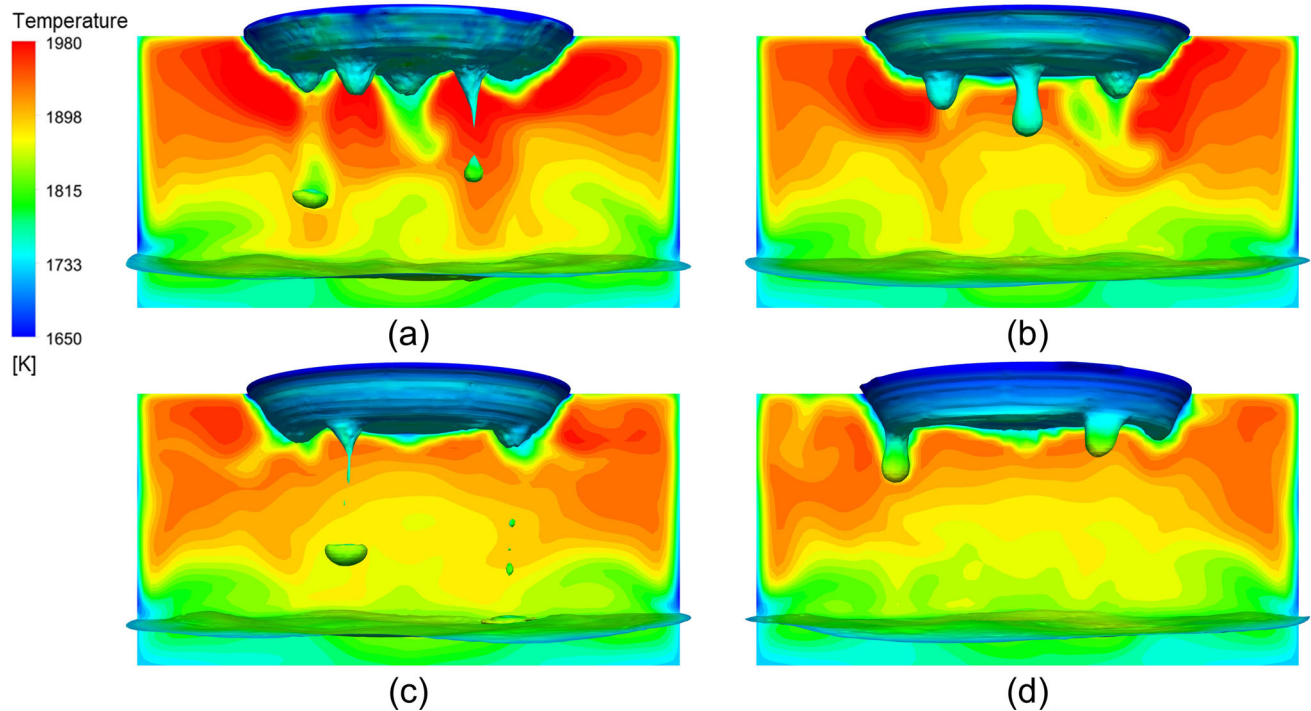


Fig. 11—Predicted temperature distribution under different electrode rotating speeds at $t_0 + 8$ s: (a) 0, (b) 20 rpm, (c) 40 rpm, and (d) 60 rpm.

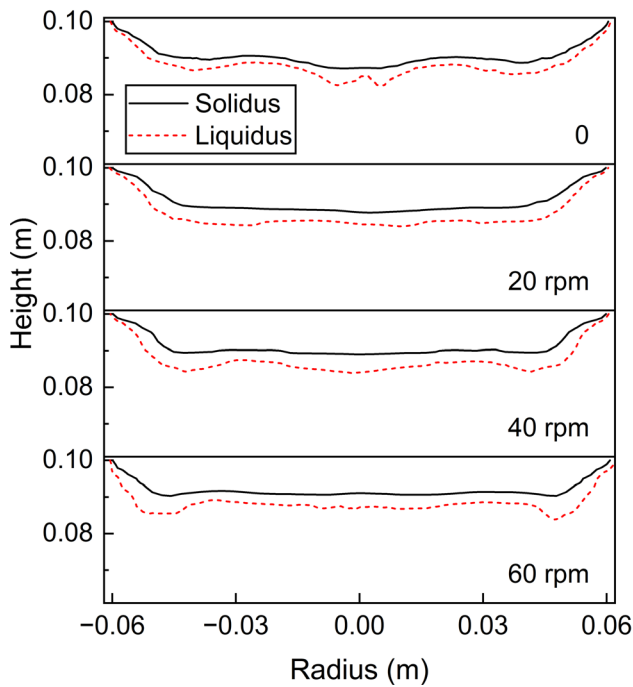


Fig. 12—Predicted shape of electrode tip under different electrode rotating speeds at $t_0 + 8$ s.

immersion depth and shape of the electrode tip. In practice, the immersion depth is typically controlled using the voltage swing or resistance swing with the assistance of PID. Improper control deteriorates the compositional homogeneity and grain structure of the ingot. The flat shape of the electrode tip enhances the response speed and stability of the ESR control system. However, the conventional ESR process with a static electrode lacks control over the shape of the electrode tip.

Figure 12 plots the electrode tip shape under different rotating speeds. The solidus and liquidus temperatures are represented by solid and dashed lines, respectively. The liquidus curves exhibit outward movement of the faucets and disappearance of the central faucet as the electrode rotating speed increases. Consequently, the middle section of the liquidus curve becomes flat, extending this effect to the solidus curve. In this study, the standard deviation is used to quantify the deviation of the solidus curve from the horizontal plane. The melting of the electrode periphery is dominated by the AC skin effect and is not included in the quantification. The standard deviations recorded with the electrode rotating at 0, 20, 40, and 60 rpm are 1.14×10^{-3} , 1.02×10^{-3} , 5.03×10^{-4} , and 3.43×10^{-4} , respectively. The electrode rotation contributes to the flattening of the electrode tip, resulting in a significant improvement of 69.9 pct at a rotating speed of 60 rpm.

ESR is known for its effective removal of inclusions from electrode metal. The majority of inclusions are removed during the formation and dripping of the droplets underneath the electrode tip, facilitated by an effective contact between the slag and metal phases.^[12] However, certain inclusions such as oxide inclusions do

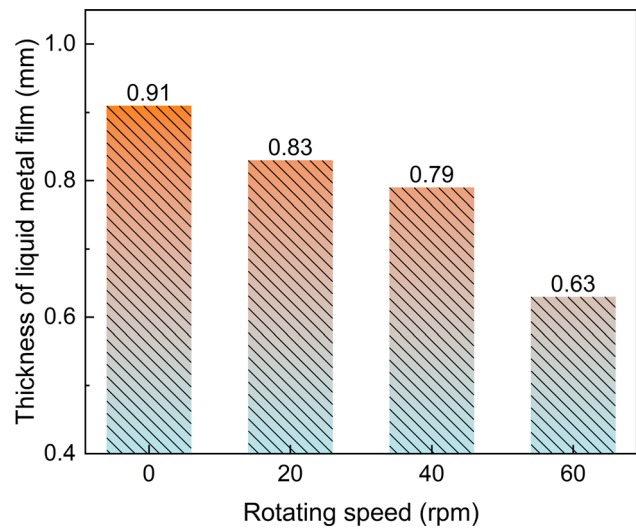


Fig. 13—Effect of electrode rotating speed on the thickness of liquid metal film at the electrode tip.

not melt with the electrode metal due to differences in melting points. The strong flow in the slag contributes to the renewal of the slag/metal interface, causing the inclusion to migrate from the melting boundary of the electrode towards the slag/metal interface, where they are subsequently absorbed by the slag. Hence, the thickness of the liquid metal film at the electrode tip plays a crucial role in the efficiency of inclusion removal. Figure 13 illustrates the impact of electrode rotating speed on the thickness. With the electrode rotating at 0, 20, 40, and 60 rpm, the thickness of liquid metal film is 0.91, 0.83, 0.79, and 0.63 mm, respectively. The rotating speed is inversely proportional to the thickness of the liquid metal film. It indicated that adjusting the electrode rotating speed can reduce the thickness by over 30.77, dramatically improving the efficiency of inclusion removal. Additionally, a thinner liquid metal film results in a larger specific surface area, providing more opportunities for inclusions to reach the slag/metal interface and improving the removal rate of harmful elements such as sulfur.

E. Droplet Behaviors

The liquid steel is refined drop by drop during the ESR process. The droplet behaviors play crucial roles in the refining efficiency and ingot quality. Figure 14 shows the formation and dripping process of droplets with static and rotating electrodes. Droplet formation starts with a dramatic thickening in the liquid metal film, *i.e.*, the faucet appears. In the case with a static electrode, as shown in Figure 14(a), the flow inside the faucet is slow, while the molten metal converges rapidly along the faucet surface towards its tip. Once the surface tension cannot withstand its own gravity, the neck shrinks. The shrinkage results in an explosive increase in the local Lorentz force, enough to pinch the neck off. Then, the slender neck breaks, resulting in the formation of a primary droplet along with satellite droplets. The primary droplet is compressed during its dripping

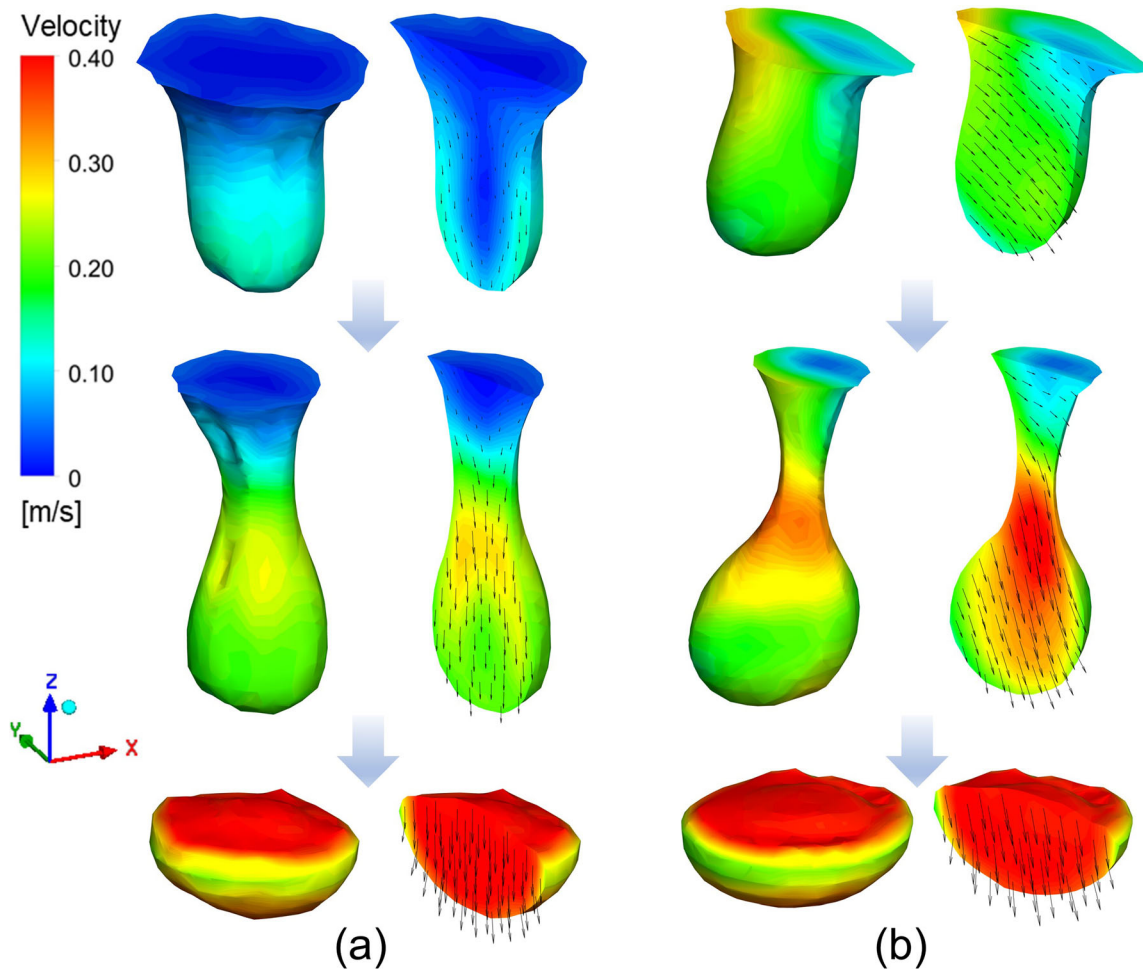


Fig. 14—Formation and dripping of droplets with static (a) and rotating (b) electrodes.

process due to the uneven distribution of velocity within it. When the electrode rotates at 60 rpm (as displayed in Figure 14(b)), noticeable inclination and horizontal velocity of the faucet can be observed. The molten metal behind the faucet moves faster and supplies the faucet due to the relative motion between the electrode and the faucet. Once the neck breaks, the droplet is thrown out, following a projectile trajectory hindered by the slag. Hence, the horizontal velocity of the droplet significantly decreases before it hits the liquid metal pool, similar to that with a static electrode.

To calculate the diameter of droplets and the melting rate of the solid electrode, a fixed horizontal plane is established to monitor the mass flow rate of the falling droplets. Figure 15 plots time-variations in the mass flow rate under different electrode rotating speeds. The mass flow rate peaks (over 10 kg/s) whenever a primary droplet passes through the monitor plane. When two primary droplets fall within a short period, the peaks may merge into a higher peak. Small fluctuations follow the peak, indicating the passage of satellite droplets through the monitor plane. As depicted, the intervals between the droplets dripping become more uniform as the rotating speed increases.

The mass of one droplet can be calculated by integrating the mass flow rate. To avoid interference from satellite droplets, small fluctuations are initially filtered out. For each case, the integration range consists of at least 20 droplets to minimize errors. The average mass of the droplets is used to calculate their equivalent diameter, as shown in Figure 16. When the electrode rotates, the centrifugal force reduces the surface tension's ability to withstand its own weight. Besides, the centrifugal force acts in the opposite direction to the Lorentz force, making it easier to break the neck of the droplet. As a result, the droplets are thrown out earlier in smaller sizes than that with a static electrode. As the electrode rotating speed increases from 0 to 60 rpm, the equivalent diameter of droplets decreases from 12.90 to 11.77 mm. This implies that increasing the electrode rotating speed can refine the droplets by up to 8.76 pct. The reduction in droplet size increases the specific surface area of droplets, facilitating the removal of inclusions and impurity elements from the steel.

The electrode melting rate can be calculated by integrating the mass flow rate per unit time. This rate is influenced by local heat convection and heat conduction. The effect of electrode rotating speed on the

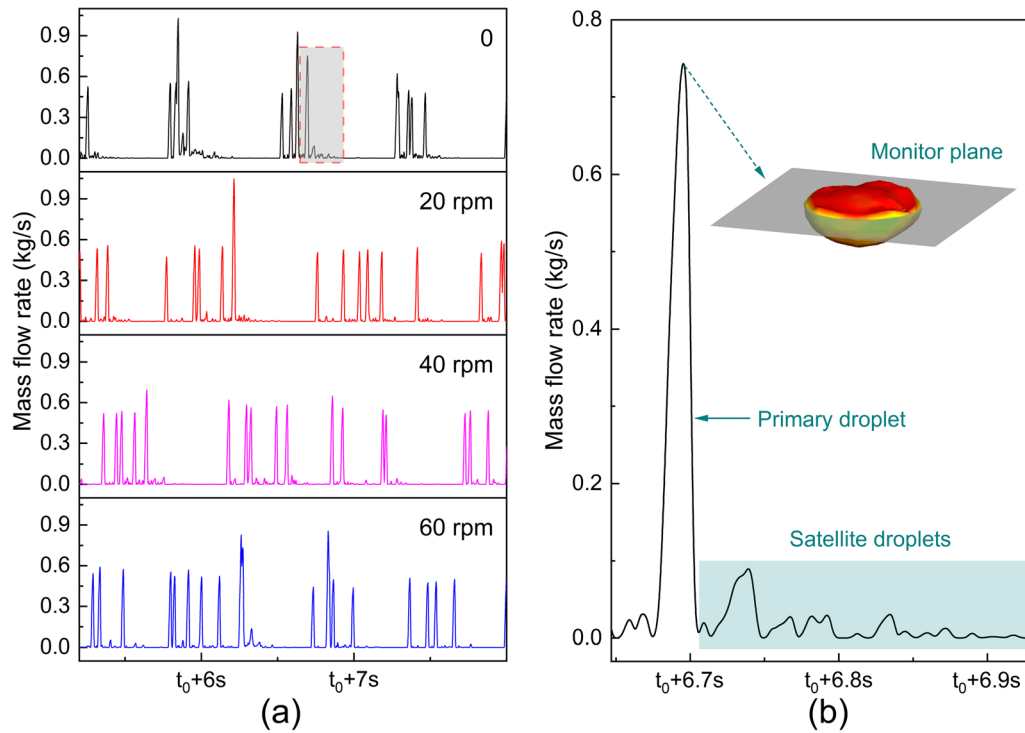


Fig. 15—Time-variations in the mass flow rate under different electrode rotating speeds (a) and detail view (b).

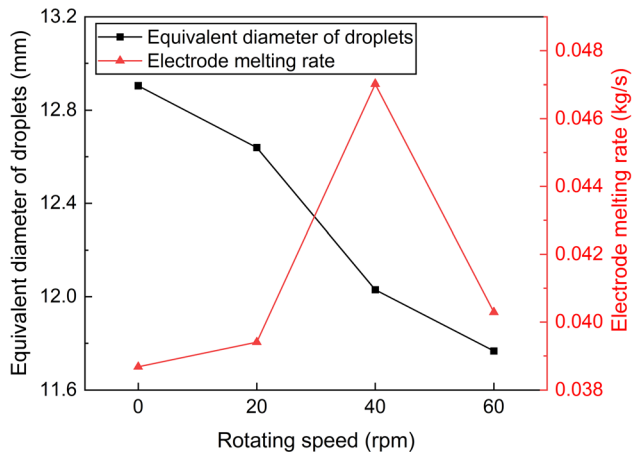


Fig. 16—Effect of the electrode rotating speed on the equivalent diameter of droplets and electrode melting rate.

melting rate depends on the competition between the effective thermal conductivity and the temperature difference (between the electrode and slag). As discussed above, the increase in the rotating speed results in an increase in the local thermal conductivity and a decrease in the slag temperature. As the electrode rotating speed increases from 0 to 40 rpm, the electrode melting rate increases from 0.0387 to 0.0470 kg/s. This is because the rotation intensifies the local flow around the electrode, resulting in that the increase in the local effective thermal conductivity dominates the competition. However, when the electrode rotating speed further increases to 60 rpm, the melting rate decreases to 0.0403 kg/s. It can be attributed to the remarkable reduction in slag

temperature. When compared to a static electrode, the melting rate, which represents the productivity of the ESR process, is improved by 1.89, 21.56, and 4.16 pct with the electrode rotating at 20, 40, and 60 rpm, respectively. The maximum productivity is achieved at 40 rpm without increasing the power input, indicating the existence of an optimal rotating speed for maximizing productivity. This finding also aligns with the conclusion reported in Reference 13.

V. CONCLUSIONS

Based on experimental verification, a multiphysics coupled model is developed to investigate the melting and rotation of the solid electrode. The model pays specific attention to the shape evolution of the electrode tip, as well as the formation and motion of droplets, in response to different electrode rotating speeds. The following conclusions are drawn.

1. The periphery of the electrode melts first due to the AC skin effect. Several randomly dispersed faucets and a central faucet form underneath the static electrode. As the electrode rotating speed increases, the faucets gradually move outwards until reaching the periphery.
2. The electrode rotation intensifies the flow in the slag layer and enhances the global heat convection and diffusion in the melt. As the rotating speed varies from 0 to 60 rpm, the averaged vorticity increases from 3.04 to 6.51 s^{-1} , while the maximum temperature decreases from 2022 K to 1953 K.

- In comparison to the case with a static electrode, at a rotating speed of 60 rpm, the standard deviation of the electrode tip profile with respect to the horizontal plane is reduced by 69.9 pct. The electrode rotation contributes to the flattening of the electrode tip, thereby enhancing the response speed and stability of the ESR control system.
- As the electrode rotating speed increases from 0 to 60 rpm, the thickness of liquid metal film decreases from 0.91 to 0.63 mm, while the equivalent diameter of droplets decreases from 12.90 to 11.77 mm. The electrode rotation increases the specific surface area, dramatically improving the removal efficiency of inclusions as well as harmful elements.
- The predicted melting rates of the electrode are 0.0387, 0.0394, 0.0470, and 0.0403 kg/s in the cases with electrode rotating at 0, 20, 40, and 60 rpm, respectively. Productivity reached a maximum of 21.56 pct at a rotating speed of 60 rpm without increasing power input.

ACKNOWLEDGMENTS

This work was supported by the National Natural Science Foundation of China (Grant No. 52104324), Fundamental Research Funds for the Central Universities (Grant No. N2325011), The National Key Research and Development Program of China (Grant No. 2022YFB3705101), and The Excellent Youth Fund of Liaoning Natural Science Foundation (Grant No. 2023JH3/10200001).

CONFLICT OF INTEREST

On behalf of all authors, the corresponding author states that there is no conflict of interest.

REFERENCES

- R. Zhang, P. Liu, C.Y. Cui, B.J. Zhang, J.H. Du, Y.Z. Zhou, and X.F. Sun: *Acta Metall. Sin.*, 2021, vol. 57, pp. 1215–28.
- L.Y. Levkov, D.A. Shurygin, S.V. Orlov, Yu.N. Kriger, A.V. Lazukin, G.A. Dudka, A.S. Lesunov, and A.S. Ronzhin: *Metallurgist*, 2014, vol. 58, pp. 677–83.
- L.Y. Levkov, M.A. Kissel'man, D.A. Shurygin, I.A. Ivanov, A.S. Lesunov, and A.V. Krasovskii: *Metallurgist*, 2018, vol. 62, pp. 738–52.
- K. Kajikawa, S. Ganesh, K. Kimura, H. Kudo, T. Nakamura, Y. Tanaka, Y. Schwant, R. Schwant, F. Gatazka, and L. Yang: *Ironmak. Steelmak.*, 2007, vol. 34, pp. 216–20.
- C.K. Cooper, D. Ghosh, D.A.R. Kay, and R.J. Pomfret: *28th Electr. Furn. Conf. Proc.*, Warrendale, PA, 1970, pp. 8–11.
- A. Mitchell: *Ironmak. Steelmak.*, 1974, vol. 1, pp. 172–79.
- Q. Wang, Y. Liu, F. Wang, G.Q. Li, B.K. Li, and W.W. Qiao: *Metall. Mater. Trans. B*, 2017, vol. 48B, pp. 2649–63.
- C.B. Shi, Y. Huang, J.X. Zhang, J. Li, and X. Zheng: *Int. J. Miner. Metall. Mater.*, 2021, vol. 28, pp. 18–29.
- S.F. Medina and A. Cores: *ISIJ Int.*, 1993, vol. 33, pp. 1244–51.
- C.B. Shi, X.C. Chen, H.J. Guo, Z.J. Zhu, and H. Ren: *Steel Res.*, 2012, vol. 83, pp. 472–86.
- Z.B. Li, W.H. Zhou, and Y.D. Li: *Iron Steel*, 1980, vol. 15, pp. 20–26.
- X.C. Huang, B.K. Li, Z.Q. Liu, X. Yang, and F. Tsukihashi: *Int. J. Heat Mass Transf.*, 2019, vol. 135, pp. 1300–11.
- I.V. Chumanov and V.I. Chumanov: *Metallurgist*, 2001, vol. 45, pp. 125–28.
- V.I. Chumanov and I.V. Chumanov: *Russ. Metall.*, 2010, vol. 6, pp. 499–504.
- C. Demirci, B. Mellinshoff, J. Schlüter, C. Wissen, M. Schwenk, and B. Friedrich: *Proc. Liq. Met. Process. Cast. Conf.*, Birmingham, UK, 2019, pp. 117–30.
- A. Kharicha, A. Ludwig, and M. Wu: *ISIJ Int.*, 2014, vol. 54, pp. 1621–28.
- H. Shi, M.J. Tu, Q.P. Chen, and H.F. Shen: *Int. J. Heat Mass Transf.*, 2020, vol. 158, p. 119713.
- L.F. Zhang, T.J. Wen, W. Chen, X.J. Li, and A.J. Xu: *Metall. Mater. Trans. B*, 2021, vol. 52B, pp. 3167–82.
- A. Kharicha, A. Ludwig, and M. Wu: *Proc. Liq. Met. Process. Cast. Conf.*, Nancy, France, 2011, pp. 41–48.
- E. Karimi-Sibaki, A. Kharicha, J. Bohacek, M. Wu, and A. Ludwig: *Metall. Mater. Trans. B*, 2015, vol. 46B, pp. 2049–61.
- H. Wang, Y.B. Zhong, Q. Li, Y.P. Fang, W.L. Ren, Z.S. Lei, and Z.M. Ren: *Metall. Mater. Trans. B*, 2017, vol. 48B, pp. 655–63.
- H. Wang, Y.B. Zhong, L.C. Dong, Z. Shen, Q. Li, W.M. Li, T.X. Zheng, W.L. Ren, Z.S. Lei, and Z.M. Ren: *JOM*, 2018, vol. 70, pp. 2917–26.
- F. Wang, Q. Wang, and B.K. Li: *ISIJ Int.*, 2017, vol. 57, pp. 91–99.
- X.C. Huang, B.K. Li, and Z.Q. Liu: *Metall. Mater. Trans. B*, 2018, vol. 49B, pp. 709–22.
- V. Weber, A. Jardy, B. Dussoubs, D. Ablitzer, S. Ryberon, V. Schmitt, S. Hans, and H. Poisson: *Metall. Mater. Trans. B*, 2009, vol. 40B, pp. 271–80.
- A.H. Dilawari and J. Szekely: *Metall. Trans. B*, 1977, vol. 8, pp. 227–36.
- C.W. Hirt and B.D. Nichols: *J. Comput. Phys.*, 1981, vol. 39, pp. 201–25.
- X.L. Li, B.K. Li, Z.Q. Liu, R. Niu, Q. Liu, X.C. Huang, G.D. Xu, and X.M. Ruan: *Steel Res. Int.*, 2019, vol. 90, p. 1800423.
- A.K. Singh, B. Basu, and A. Ghosh: *Metall. Mater. Trans. B*, 2006, vol. 37B, pp. 799–809.
- J.U. Brackbill, D.B. Kothe, and C. Zemach: *J. Comput. Phys.*, 1992, vol. 100, pp. 335–54.
- Z.Q. Liu, R. Niu, Y.D. Wu, B.K. Li, Y. Gan, and M.H. Wu: *Int. J. Heat Mass Transf.*, 2021, vol. 173, p. 121237.
- Y. Liu, Z. Zhang, G.Q. Li, Y. Wu, D.M. Xu, and B.K. Li: *Vacuum*, 2018, vol. 158, pp. 6–13.
- Z.B. Li: *Electroslag Metallurgy Theory and Practice*, Metallurgical Industry Press, Beijing, 2010.
- X.C. Huang, Z.Q. Liu, Y.R. Duan, C.J. Liu, and B.K. Li: *J. Mater. Res. Technol.*, 2022, vol. 20, pp. 3843–59.

Publisher's Note Springer Nature remains neutral with regard to jurisdictional claims in published maps and institutional affiliations.

Springer Nature or its licensor (e.g. a society or other partner) holds exclusive rights to this article under a publishing agreement with the author(s) or other rightsholder(s); author self-archiving of the accepted manuscript version of this article is solely governed by the terms of such publishing agreement and applicable law.